Mn incorporation in as-grown and annealed (Ga,Mn)As layers studied by x-ray diffraction and standing-wave fluorescence

V. Holý,[1] Z. Matěj,[1] O. Pacherová,[2] V. Novák,[2] M. Cukr,[2] K. Olejník,[2] and T. Jungwirth[2,3]
[1]*Faculty of Mathematics and Physics, Department of Electronic Structures, Charles University, Ke Karlovu 5, 121 16 Prague 2, Czech Republic*
[2]*Institute of Physics ASCR, Cukrovarnická 10, 162 53 Praha 6, Czech Republic*
[3]*School of Physics and Astronomy, University of Nottingham, Nottingham NG7 2RD, United Kingdom*
(Received 4 September 2006; published 11 December 2006)

A combination of high-resolution x-ray diffraction and a technique of x-ray standing-wave fluorescence at grazing incidence is employed to study the structure of a (Ga,Mn)As-diluted magnetic semiconductor and its changes during post-growth annealing steps. We find that the film is formed by a uniform, single-crystallographic phase epilayer covered by a thin surface layer with enhanced Mn concentration to Mn atoms at random noncrystallographic positions. In the epilayer, Mn incorporated at the interstitial position has a dominant effect on lattice expansion as compared to substitutional Mn. The expansion coefficient of interstitial Mn estimated from our data is consistent with theory predictions. The concentration of interstitial Mn and the corresponding lattice expansion of the epilayer are reduced by annealing, accompanied by an increase of the density of randomly distributed Mn atoms in the disordered surface layer. Substitutional Mn atoms remain stable during the low-temperature annealing.

DOI: 10.1103/PhysRevB.74.245205 PACS number(s): 61.10.Nz, 75.50.Pp, 68.49.Uv

I. INTRODUCTION

Mn is incorporated in ferromagnetic (Ga,Mn)As semiconductors in substitutional Mn_{Ga} positions and, a fraction of Mn atoms can also occupy interstitial sites surrounded by four Ga ($Mn_i^{(1)}$) or four As ($Mn_i^{(2)}$) nearest neighbors, as illustrated in Fig. 1. Substitutional Mn_{Ga} ions provide local magnetic moments and holes that mediate long-range ferromagnetic coupling between the local moments.[1,2] The less energetically favorable Mn_i donors[3,4] occur due to the tendency to self-compensation in the highly Mn-doped GaAs host with nearly covalent crystal bonding. Mn_i impurities are detrimental to ferromagnetism since they act as charge and moment compensating defects.[5–9]

The concentration of Mn_i in (Ga,Mn)As epilayers can be significantly reduced by low-temperature (~200 °C) post-growth annealing which leads to a dramatic improvement of ferromagnetic properties of the epilayers.[3,10–13] For example, in the material with 9% nominal Mn doping which holds the current record Curie temperature, the paramagnetic-to-ferromagnetic transition was moved from 95 K in the as-grown material up to 173 K after annealing.[8] Detailed analysis of Mn incorporation in (Ga,Mn)As and of the process of Mn_i removal by annealing has therefore been one of the key topics in materials research of these dilute moment ferromagnetic semiconductors.

Direct experimental evidence for the presence of interstitial Mn impurities in as-grown (Ga,Mn)As epilayers and for their reduced density after post-growth annealing was given by combined channeling Rutherford backscattering and particle-induced x-ray emission measurements.[3] The technique can distinguish between Mn_i and Mn_{Ga} by counting the relative number of exposed Mn atoms and the ones shadowed by lattice site host atoms at different channeling angles. Mn incorporation at different crystallographic positions was also studied by x-ray absorption[14] and by high-resolution diffraction and structure factor measurements.[15,16] The extraction of partial concentrations of different types of Mn impurities in the lattice by these techniques is less straightforward as the data are sensitive not only to the crystallographic positions of Mn but also to local lattice distortions on neighboring sites. X-ray diffraction measurement of the (Ga,Mn)As epilayer lattice parameter is another indirect technique that has been used to monitor the decrease of Mn_i concentration in the epilayer after annealing.[17–19] Here the interpretation has relied on the assumption that Mn_i are the only mobile impurities during the annealing process[6,20,21] and used[17] theoretical values[22] for the defect expansion coefficients in (Ga,Mn)As or assumed[19] specific scenarios for charge compensation that fulfill the overall charge neutrality condition.

A series of experimental works, including resistance-monitored annealing combined with Auger spectroscopy,[7] depth profiling by x-ray reflectometry,[23] and surface capping experiments,[13,24–26] have focused on the mechanism causing the decrease of Mn_i concentration in annealed (Ga,Mn)As epilayers. The studies suggest that Mn_i impurities outdiffuse to the layer surface and are passivated by oxygen when an-

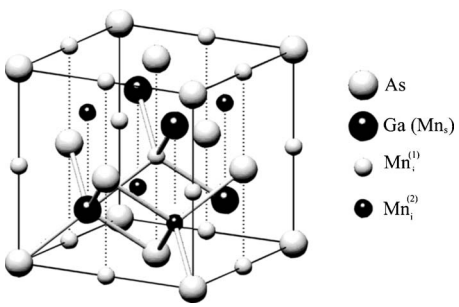

FIG. 1. The elementary unit cell of GaAs with possible positions of Mn atoms. The interstitial atoms $Mn_i^{(2)}$ have the same lateral coordinates as the substitutional Mn atoms.

nealed in air or by forming MnAs in case of (Ga,Mn)As films overgrown by As capping layers.

In this paper we report on high-resolution x-ray diffraction[27] (XRD) experiments and measurements of x-ray standing-wave[28] (XSW) fluorescence at grazing incidence in as-grown and annealed (Ga,Mn)As films. The former technique allows us to monitor changes in the abundance of different types of impurities in the ordered part of the epilayer during annealing steps by determining individual contributions from the impurities to the lattice parameter. XSW at grazing incidence is an experimental technique which we developed for detecting lattice-site-resolved Mn fluorescence from pseudomorphic (Ga,Mn)As thin films. By small variations in the incidence angle of the primary beam we can tune the exposure from covering the entire epilayer to only a few-nanometer-thin surface layer. Data collected by the two complementary techniques are interpreted directly with no *a priori* assumptions on the behavior of Mn in as-grown systems and during annealing. They are used to determine crystal phases in the (Ga,Mn)As layers, to compare lattice expansion contributions from Mn_{Ga} and Mn_i, to give an estimate for the Mn_i lattice expansion coefficient, to compare stabilities of Mn_{Ga} and Mn_i atoms during annealing, and to directly monitor Mn_i outdiffusion from the (Ga,Mn)As epilayer to the surface and to characterize the surface Mn incorporation.

The paper is organized as follows. In Sec. II we briefly introduce the sample growth and characterization and experimental setups. Because of the novelty of the grazing incidence XSW technique, we derive in Sec. III expressions for the fluorescence intensity in this geometry and show typical numerical spectra used for fitting the experimental data. Results of XSW and XRD measurements and their comparison with theory are presented in Sec. IV. In Sec. V we discuss our results in the context of previous and potential future measurements, and we conclude in Sec. VI with a brief summary of our main findings.

II. EXPERIMENT

Four samples were studied from a wafer grown by molecular-beam epitaxy (MBE) on a (001) GaAs semi-insulating substrate. The MBE deposition started with a 320-nm-thick high-temperature GaAs buffer followed by a 5-nm low-temperature GaAs layer and, finally, a low-temperature (Ga,Mn)As epilayer was grown with a nominal thickness of 100 nm. The substrate temperature during the low-temperature deposition was 240 °C as measured by a floating thermocouple. Mn doping of $3.5\% \pm 0.5\%$ was estimated from the ratio of the growth rates measured by the reflection high-energy electron diffraction (RHEED) oscillations before and after opening the Mn cell. The as-grown structure (sample No. 1) shows metallic conductivity with room-temperature conductivity of 300 $\Omega^{-1}\,\mathrm{cm}^{-1}$. The Curie temperature of 55 K was determined by superconducting quantum interference device (SQUID) magnetization measurements. Samples Nos. 2, 3, and 4 were annealed in air at 200 °C for 1, 2, and 4 h, respectively. Corresponding Curie temperatures are 65 K, 68 K, and 72 K.

Room-temperature XRD measurements of the thickness of (Ga,Mn)As epilayers and of the contributions to the lattice parameter from different types of impurities were performed for coplanar symmetric 002 and 004 diffractions. We used a commercial high-resolution diffractometer equipped with conventional Cu $K\alpha$ x-ray tube, parabolic x-ray mirror, Bartels-type 4×220 Ge monochromator, and 3×220 Ge analyzing crystal.

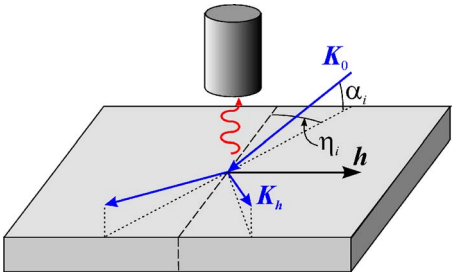

FIG. 2. (Color online) Sketch of the grazing-incidence geometry. The wavy line is the fluorescence radiation; the dashed line denotes the diffracting crystallographic plane perpendicular to the sample surface.

XSW fluorescence experiments were carried out on the ID32 beamline at the European Synchrotron Radiation Facility in Grenoble using an energy of the primary x-ray beam of 10 keV. The technique is based on interference of the primary x-ray beam with the diffracted beam which creates a standing wave in the diffracting crystal volume. The period of the standing-wave pattern equals the distance of the diffracting net planes, and the position of the antinodes of the standing wave can be sensitively tuned by changing the direction of the primary beam.[28,29] The presence of Mn atoms in different lattice positions was detected by measuring the fluorescent Mn$K\alpha$ radiation. The solid-state detector was placed close to the sample surface, collecting the fluorescence signal from a wide solid angle, yet avoiding direct illumination of the detector by the primary and diffracted beams.

The XSW experimental setup is schematically illustrated in Fig. 2. For in-plane 400, 220, 200, and 420 diffractions and for various incidence angles α_i near the critical angle α_c of total external reflection, we measured the dependence of the fluorescence signal Φ on the azimuthal deviation $\delta\eta_i$ of the primary x-ray beam from the diffraction position. Recall that (Ga,Mn)As epitaxial layers grown on GaAs buffer have a pseudomorphic structure—i.e., their in-plane lattice parameter is the same as in the substrate—however, their vertical lattice parameters are different. Therefore, the XSW experiment has to be carried out in the grazing incidence ($\alpha_i \sim \alpha_c$) geometry. In this arrangement the diffracting net planes and the antinode planes of the standing wave are perpendicular to the surface, allowing only for the determination of the in-plane coordinates of Mn atoms.

To our knowledge this technique has not yet been employed and we therefore included the following theory section which details the procedures for analyzing grazing incidence XSW data.

III. THEORY

In the calculation of the fluorescence intensity we assume that the intensity of the fluorescence radiation emitted from a

given atom is proportional to the magnitude of the Poynting vector

$$\mathbf{S} = \frac{1}{2}\,\mathrm{Re}(\mathbf{E} \times \mathbf{H}^*) \tag{1}$$

of the wave field inside the (Ga,Mn)As layer in the position of a given Mn atom. For the calculation of the electric and magnetic intensities **E** and **H** we use the two-beam approximation of dynamical diffraction theory.[30] In this approximation, the wave field inside the layer can be written as a superposition of four transmitted waves ($\mathbf{E}_{0n}$, $n=1,\ldots,4$) and four diffracted waves ($\mathbf{E}_{\mathbf{h}n} \equiv c_n \mathbf{E}_{0n}$, $n=1,\ldots,4$) with wave vectors $\mathbf{k}_{0n}$ and $\mathbf{k}_{\mathbf{h}n}=\mathbf{k}_{0n}+\mathbf{h}$, respectively; **h** is the diffraction vector which is assumed to be parallel to the surface. In the following, we restrict our discussion to *S* polarization in which the **E** waves are nearly perpendicular to the sample surface.

Using the Maxwell equation

$$\mathbf{H} = \frac{1}{\omega\mu_0}\mathrm{rot}\mathbf{E}$$

(μ_0 is the vacuum permeability, and ω is the frequency of the primary x-ray radiation) we obtain the following expression for the Poynting vector:

$$\mathbf{S} = S_0\mathbf{t}_0 + S_\mathbf{h}\mathbf{t}_\mathbf{h}, \tag{2}$$

where $\mathbf{t}_{0,\mathbf{h}}$ are the unit vectors parallel to the in-plane components of the wave vectors of the primary and diffracted waves, respectively, and

$$S_0(\phi,Z) = \frac{K}{2\mu_0\omega}\,\mathrm{Re}\left[\sum_{n,m=1}^{4} \mathrm{e}^{\mathrm{i}Z(k_{0nz}-k^*_{0mz})} E_{0n}E^*_{0m}(1+c_n\mathrm{e}^{\mathrm{i}\phi})\right],$$

$$S_\mathrm{h}(\phi,Z) = \frac{K}{2\mu_0\omega}\,\mathrm{Re}\left[\sum_{n,m=1}^{4} \mathrm{e}^{\mathrm{i}Z(k_{0nz}-k^*_{0mz})} E_{0n}E^*_{0m}c^*_m(1+c_n\mathrm{e}^{-\mathrm{i}\phi})\right] \tag{3}$$

are the components of the Poynting vector parallel to the primary and diffracted beams, respectively. Since the amplitudes E_{0n} and $E_{\mathbf{h}n}$ depend on the depth *Z* of the Mn atom below the surface, the entire Poynting vector depends on *Z* as well. In Eqs. (3), $\phi=\mathbf{h}\cdot\mathbf{r}$, where **r** is the position of the Mn atom within the GaAs unit cell. Parameters E_{0n}, c_n, and k_{0nz} were calculated from the two-beam dynamical diffraction theory taking into account four tie points on the dispersion surface.[30,27]

The fluorescence signal is proportional to the weighted sum of the contributions of all Mn atoms:

$$\Phi = \mathrm{const} \times \int_{-\infty}^{0} \mathrm{d}Z\mathrm{e}^{-\mu_f|Z|}\sum_p n_p(Z)|\mathbf{S}(\phi_p,Z)|, \tag{4}$$

where μ_f is the linear absorption coefficient of the Mn $K\alpha$ fluorescence radiation in GaAs and $n_p(Z)$ is the concentration profile of the particular impurity in the (Ga,Mn)As epilayer normalized to 1 ($p=\mathrm{s},\mathrm{i}^{(1)},\mathrm{i}^{(2)}$)—e.g., $n_s=1$ for substitutional Mn occupying all Ga sites. Equation (4) is the basis for numerical simulations; the resulting fluorescence signal Φ is convoluted with the angular distributions of the primary beam intensity both in the azimuthal direction and in the direction perpendicular to the sample surface. The fluorescence signal for randomly distributed Mn atoms, $\mathrm{Mn_r}$, is simulated numerically by averaging the value of Φ obtained from Eq. (4) over all values of the phase ϕ. Note that $\mathrm{Mn_r}$ atoms can represent another phases present in the sample (MnAs for instance) or can be incorporated, e.g., in an amorphous surface oxide layer.

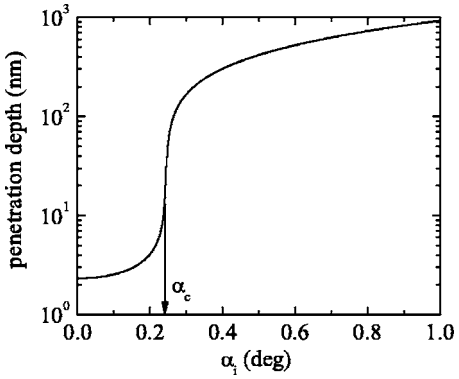

FIG. 3. The dependence of the penetration depth of the primary x-ray beam on the incidence angle α_i in GaAs calculated the energy of 10 keV; α_c denotes the critical angle of total external reflection.

An important advantage of the grazing-incidence geometry is that the penetration depth of the primary x-ray radiation can be sensitively tuned by changing its incidence angle α_i, as shown in Fig. 3. Slightly below the critical angle α_c ($\alpha_c \approx 0.24°$ in GaAs for 10 keV beam energy) the penetration depth is only a few nanometers so that the fluorescence signal stems from Mn atoms in a very thin surface layer. When crossing the critical angle the penetration depth steeply increases and for α_i only slightly larger than α_c it exceeds 100 nm which is the thickness of the studied (Ga,Mn)As layer.

Figure 4 shows the fluorescence signal calculated for substitutional $\mathrm{Mn_{Ga}}$, for interstitial $\mathrm{Mn_i^{(1)}}$, and for $\mathrm{Mn_r}$ positions. Note that for the (001) surface orientation, $\mathrm{Mn_i^{(2)}}$ have the same lateral position as $\mathrm{Mn_{Ga}}$ and, therefore, these two impurities cannot be distinguished by measuring XSW fluorescence in the grazing incidence geometry. The theoretical fluorescence signal is plotted as a function of the azimuthal deviations $\delta\eta_i$ of the primary x-ray beam from the diffraction maximum for several incidence angles $\alpha_i=[0.20°, 0.22°, 0.24°, 0.26°, 0.28°]$ near the critical angle. The calculations were performed for in-plane 400, 220, 200, and 420 diffractions, assuming that the Mn atoms are homogeneously distributed over the whole width of the (Ga,Mn)As layer. The energy of the primary beam considered in the calculations is 10 keV. The theory curves illustrate that substitutional and random positions can be identified mainly from the strong 400 and 220 diffractions while the $\mathrm{Mn_i^{(1)}}$ positions from the weak 200 or 420 diffractions.

In Fig. 5 we plot the calculated dependence of the fluorescence signal on the incidence angle α_i far from the diffraction position. Since the signal here is excited by the transmitted wave, its α_i dependence is determined only by

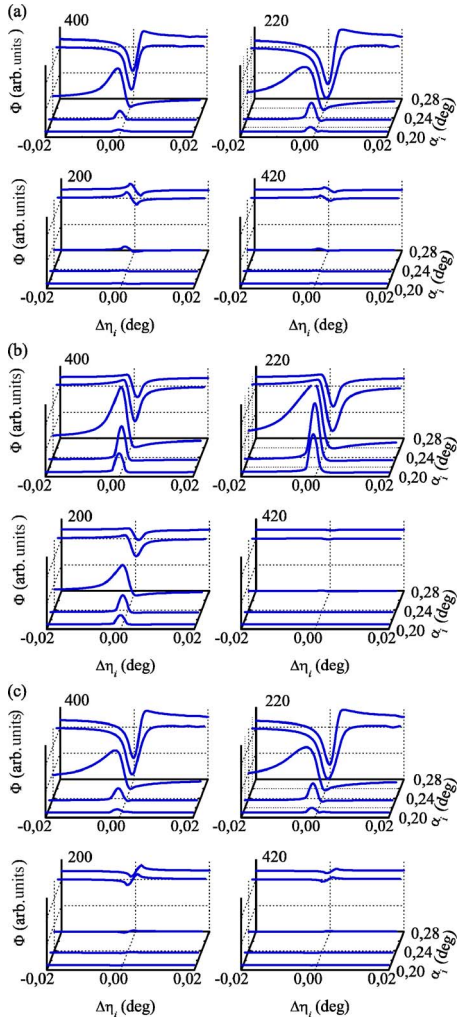

FIG. 4. (Color online) The Mn $K\alpha$ fluorescence intensities calculated for the Mn atoms in substitutional positions (or in $Mn_i^{(2)}$) (a), in the random positions Mn_r (b), and in the $Mn_i^{(1)}$ positions (c), in four in-plane diffractions 400, 220, 200, and 420 [surface (001)].

the penetration depth of the incoming radiation. Indeed, below the critical angle the calculated fluorescence is very weak while it steeply increases for $\alpha_i > \alpha_c$. Note that the shape of the curve does not depend on the position of Mn atoms in the unit cell. To illustrate the sensitivity of the α_i dependence of the fluorescence on inhomogeneities in the Mn depth profile, two curves are plotted in Fig. 5; the solid line corresponds to a uniform Mn distribution within the whole 100-nm-thick (Ga,Mn)As layer, and the dashed line was obtained assuming a 10-nm Mn-rich surface layer with a $10\times$ larger Mn density.

IV. RESULTS

We now present and analyze experimental data measured in the four (Ga,Mn)As layers. Since the collected fluorescence data provide more direct information on Mn positions in the lattice and allow us to study both the ordered epilayer part of the (Ga,Mn)As film and the more disordered surface layer, we start with this technique. Results of the XSW experiments are also used to make a more detailed interpretation of the XRD measurements of the (Ga,Mn)As epilayer which are presented in the following subsection. As will become clear by the end of this section the two techniques, however, are largely complementary and both essential for the conclusions we arrived at in this work.

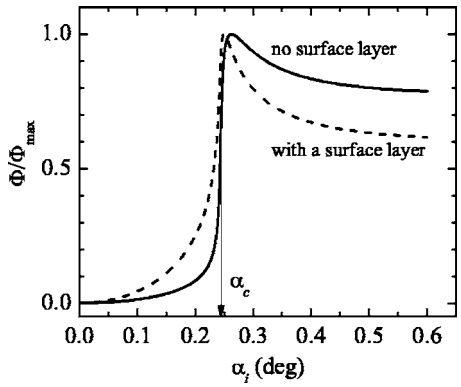

FIG. 5. The dependence of the fluorescence signal on the incidence angle α_i calculated for the azimuthal direction of the primary beam far from the diffraction position assuming a homogeneous distribution of Mn atoms (solid line) and a surface layer 10 nm thick, where the Mn density is 10 times larger (dashed line). The curves do not depend on the positions of the Mn atoms in the unit cell and on the diffraction used. α_c is the critical angle of total external reflection; the curves are normalized to their maxima.

A. X-ray standing-wave fluorescence from Mn atoms

Before resorting to the more elaborate standing-wave experiments, the role of the surface during annealing can be tested by fluorescence measurements without the XSW effect—i.e., for large azimuthal deviations $\delta\eta_i$ from the diffraction maximum. The comparison of experimental data shown in Fig. 6 with theoretical curves in Fig. 5 clearly indicates the development of a Mn-rich surface layer during the annealing process. The experimental curves could be equally well fitted assuming the thickness of the Mn-rich layer between 2 and 10 nm; the fitted surface density then increases correspondingly to the decrease of the assumed

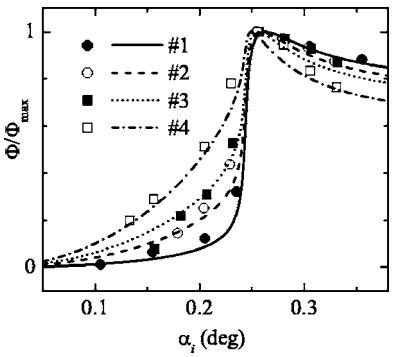

FIG. 6. The fluorescence signal measured for large angular deviations $\delta\eta_i$ from the diffraction maximum for various incidence angles (points) and its theoretical fit (lines). The curves are normalized to their maximum values.

TABLE I. The parameters obtained from the measured XSW curves. N/n is the ratio of the total Mn density in the surface layer and the total Mn density $n=3.5\%$ in the homogeneous epilayer beneath the surface layer. p_r and $p_i^{(1)}$ are the densities of Mn_r and $Mn_i^{(1)}$, respectively, relative to the density of Mn_{Ga} plus $Mn_i^{(2)}$ atoms, obtained from the XSW data at $\alpha_i > \alpha_c$. P_r is the relative density of Mn_r obtained for $\alpha_i < \alpha_c$. $q_s + q_i^{(2)}$ and q_r are the recalculated partial concentrations of Mn_{Ga} plus $Mn_i^{(2)}$ and of Mn_r, respectively, for $\alpha_i > \alpha_c$; Q_r is the recalculated partial concentration of Mn_r for $\alpha_i < \alpha_c$ (see the text for more details).

Sample No.	N/n	p_r	$p_i^{(1)}$	P_r	$q_s+q_i^{(2)}$	q_r	Q_r
1	1.1±0.1	0.12±0.01	0.04±0.01	2±1	0.865	0.1	0.62
2	5±2	0.22±0.01	0.025±0.05	5±1	0.80	0.18	0.825
3	12±3	0.28±0.05	0.035±0.01	8±2	0.76	0.21	0.88
4	17±3	0.36±0.10	0.06±0.01	15±4	0.705	0.255	0.935

surface layer thickness. This ambiguity partly hinders quantitative interpretation; nevertheless, the Mn-rich surface layer in annealed samples is ubiquitous. As an illustration we give in Table I values of the fitted surface Mn density N relative to the density n in the homogeneous epilayer beneath the surface layer assuming a fixed Mn-rich layer thickness of 3 nm for all four samples.

The origin of Mn atoms arriving at the surface during annealing and their incorporation in the surface layer is elucidated by the fluorescence measurements in the grazing-incidence XSW geometry. Examples of the measured $\Phi(\delta\eta_i)$ curves for $\alpha_i > \alpha_c$ and $\alpha_i < \alpha_c$ are shown in Figs. 7 and 8, respectively. For the incidence angle $\alpha_i \approx 0.35° > \alpha_c$ the penetration depth of the primary beam is much larger than 100 nm; i.e., the XSW signal is averaged over the entire layer volume. The XSW curves in Fig. 7 were fitted for all diffractions simultaneously, and from the fit we could determine the density p_r of Mn_r relative to the density of the substitutional Mn_{Ga} atoms plus $Mn_i^{(2)}$ atoms, $p_r = \bar{n}_r/(\bar{n}_s + \bar{n}_i^{(2)})$, and the relative density of $Mn_i^{(1)}$, $p_i^{(1)} = \bar{n}_i^{(1)}/(\bar{n}_s + \bar{n}_i^{(2)})$. Because of the large penetration depth of the incidence beam, the quantities represent average densities over the entire (Ga,Mn)As layer.

A similar fitting procedure was applied to data measured at $\alpha_i < \alpha_c$, shown in Fig. 8. Here the penetration depth of the primary beam is only 3 nm so the fitted densities correspond to a thin surface layer. The Mn_r atoms with high surface density were detected even at this small incidence angle; however, the data were not sensitive enough to measure the $Mn_i^{(1)}$ impurities. For the fitting we used the values for the relative $Mn_i^{(1)}$ densities from the measurements at $\alpha_i > \alpha_c$ and determined only the relative density P_r of Mn_r in the surface layer.

Results of the XSW experiments are summarized in Table I. For convenience we also included in the table the partial Mn impurity concentration recalculated relatively to the total combined density of Mn_{Ga}, $Mn_i^{(2)}$, $Mn_i^{(1)}$, and Mn_r, for both $\alpha_i < \alpha_c$ and $\alpha_i > \alpha_c$. In particular, we show the values of the bulk relative densities

$$q_r = \frac{\bar{n}_r}{\bar{n}} = \frac{p_r}{1 + p_r + p_i^{(1)}}, \quad q_s + q_i^{(2)} = \frac{\bar{n}_s + \bar{n}_i^{(2)}}{\bar{n}} = \frac{1}{1 + p_r + p_i^{(1)}},$$

and the relative density of the Mn_r atoms in the surface layer,

$$Q_r = \frac{P_r}{1 + P_r + p_i^{(1)}}.$$

From the data in Table I we can draw the following conclusions: (i) The number of Mn_r atoms systematically increases with annealing time. (ii) Since P_r/p_r is similar to the ratio between the (Ga,Mn)As layer thickness and the exposed surface layer width in the $\alpha_i < \alpha_c$ experiment, Mn_r atoms are concentrated in the surface layer. This also means a marginal role (if any) of second phases in the (Ga,Mn)As epilayer. (iii) As the Mn_r atoms fill the surface, the density of Mn_{Ga} plus $Mn_i^{(2)}$ impurities in the (Ga,Mn)As layer decreases. The XRD data discussed in the following subsection show that the density of substitutional Mn_{Ga} atoms remains constant during annealing. We can, therefore, directly link the outdiffusion of interstitial $Mn_i^{(2)}$ from the (Ga,Mn)As with the buildup of the Mn_r-rich surface layer. Note that we detected only a small density of $Mn_i^{(1)}$ impurities and no systematic behavior during annealing can be extracted from the data.

B. X-ray diffraction from (Ga,Mn)As epilayers

Experimental XRD curves, along with their fits obtained by conventional dynamical diffraction theory, are shown in Fig. 9. The 002 and 004 diffractions were fitted simultaneously. Local distortions of the lattice around Mn_s and $Mn_i^{(1,2)}$ atoms were neglected in the fitting procedure. The very good correspondence of experimental and theoretical diffraction curves demonstrates good structural quality of the epilayers and homogeneity of the Mn distribution. No measurable Mn concentration gradients were detected across the epilayer.

The epilayer thickness and the total lattice expansion parameter ξ, defined as $a = a_0 + \xi$ where a_0 is the GaAs lattice constant and a is the relaxed lattice parameter of the (Ga,Mn)As epilayer, were obtained independently with error bars smaller than 1%. Since the average structure factor and consequently the heights of the layer maxima on the diffraction curves depend on the impurity type, we were able to measure lattice expansion contributions from individual impurities, albeit with smaller accuracy. In particular, we assumed that $\xi = \xi_s + \xi_i + \xi_a$, where the subscript "s" stands for substitutional Mn_{Ga}, "i" for interstitial Mn of both types $Mn_i^{(1)}$ and $Mn_i^{(2)}$, and we also included antisite As_{Ga} impurities (ξ_a). Note that

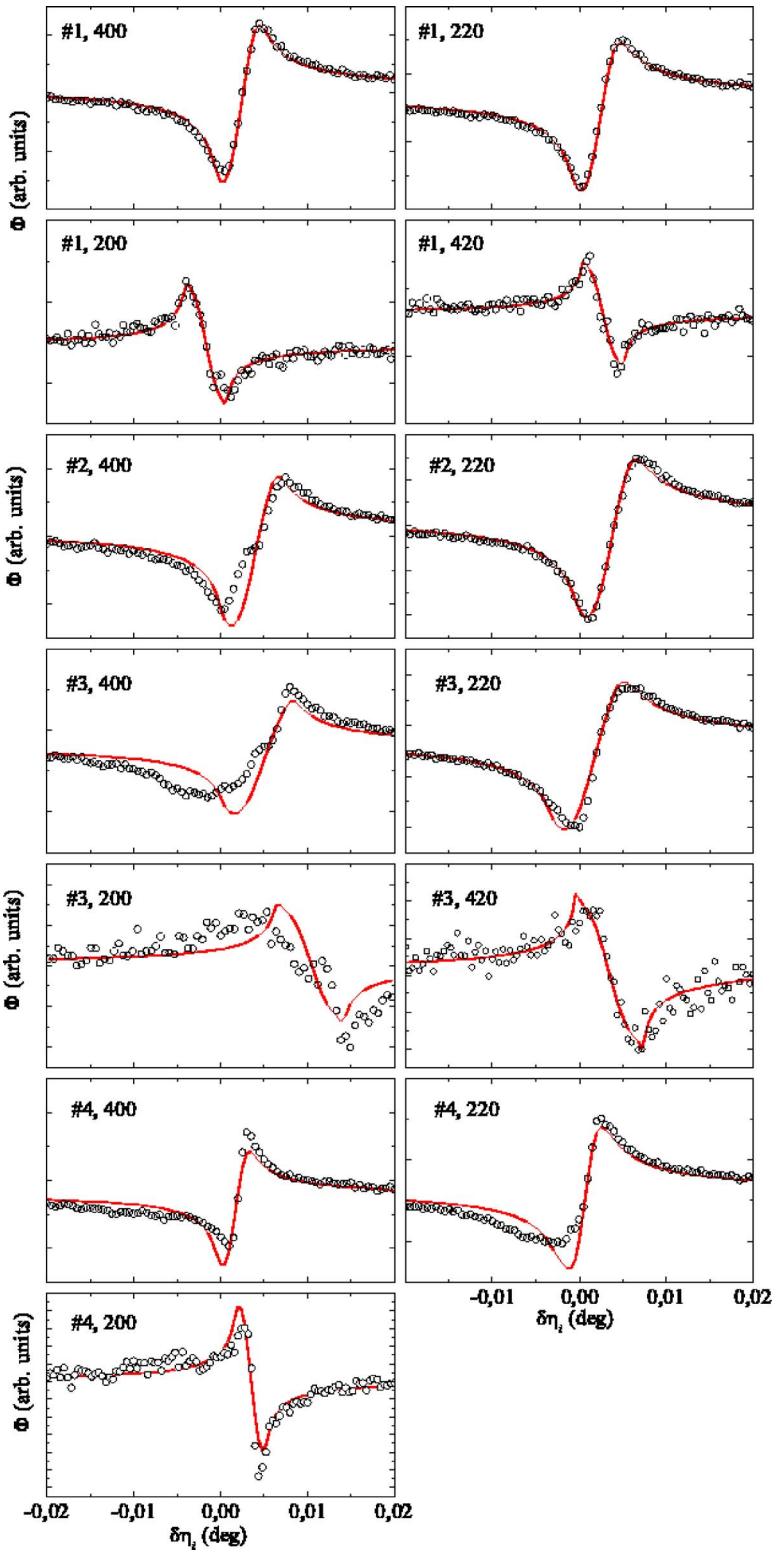

FIG. 7. (Color online) The XSW scans of samples Nos. 1–4 measured in various in-plane diffractions for the incidence angle $\alpha_i \approx 0.35°$ ($>\alpha_c$) (black points) and their theoretical fits (red lines).

the expansion parameters ξ_p, $p=\mathrm{s,i,a}$, and the Vegard's law dilatation coefficients β_p are related as $\xi_p=\beta_p n_p$.

The influence of Mn_r atoms on ξ was not taken into account in our simulations. Other crystallographic phases, where Mn_r atoms are incorporated, could affect the mean lattice constant of the epilayer only if they deform the surrounding crystal lattice and give rise to measurable diffuse x-ray scattering. Consistent with the results of XSW experiments, no such effects were detected in the XRD data for the studied (Ga,Mn)As epilayers.

We found that equally good fits could be obtained assuming any value of ξ_a ranging from 0 to 5×10^{-3} Å. The extracted total expansion ξ, shown in Table II, is independent of the choice of ξ_a which immediately implies the dependence of the fitted ξ_s and ξ_i on ξ_a. In Table II we show expansion parameters obtained for the two limiting values of

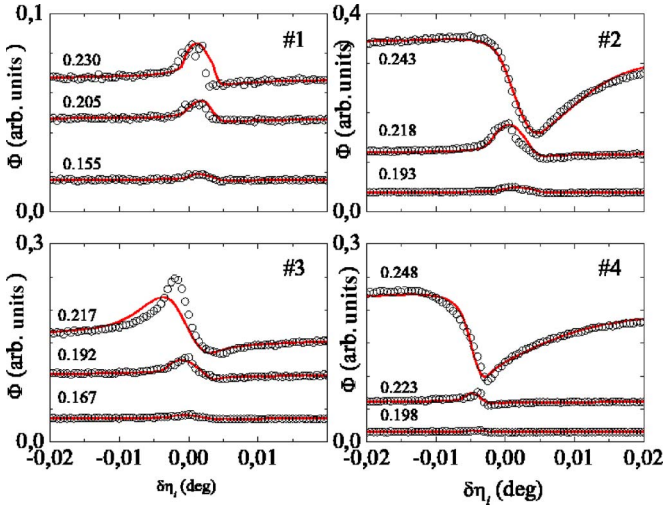

FIG. 8. (Color online) The XSW scans of samples Nos. 1–4 measured in the 220 in-plane diffraction for three incidence angle smaller or close to the critical angle α_c (black points) and their theoretical fits (red lines). The values of the incidence angle α_i in degrees are indicated above the corresponding curve.

ξ_a. Despite the quantitative ambiguities in the values of individual expansion parameters we can safely conclude that the lattice constant decreases during annealing and that the density of Mn_{Ga} atoms remains constant and, consequently, the decrease of the total lattice parameter with annealing time is due to the removal of Mn_i impurities from the ordered epilayer part of the (Ga,Mn)As film. (Note that As_{Ga} antisites in GaAs are stable up to ~450 °C.[21])

Although the XRD and XSW experiments did not allow us to separately determine Mn_{Ga} and Mn_i partial densities, the *p*-type character of the (Ga,Mn)As semiconductor and the single acceptor nature of Mn_{Ga} and the double-donor nature of Mn_i and of As_{Ga} imply that $n_s > 2n_i$. From this and from the expansion parameters in Table II we obtain that the dilatation coefficient β_i is at least 10× larger than β_s. A significantly larger lattice expansion due to Mn_i as compared to Mn_{Ga} is consistent with *ab initio* theory predictions.[22,31]

Using the results of XSW measurements and recalling that Mn_i are the only unstable impurities during annealing which contribute to ξ we can also make an estimate for the absolute value of β_i. The measured changes in ξ after each annealing step and the Mn_i expansion coefficient are related as $\beta_i = \Delta\xi_i / \Delta n_i$, where $\Delta n_i = n[\Delta q_i^{(1)} + \Delta(q_s + q_i^{(2)})]$. For n we can take the MBE-growth value 3.5% ± 0.5% and the changes of the relative partial concentrations can be read out from Table I. The value $\beta_i = 0.4 \pm 0.2$ we arrive at has an appreciable scatter, reminiscent of the current theoretical uncertainty for this coefficient.[22,31] Nevertheless, the experiment and theory are consistent within these error bars.

V. DISCUSSION

Our experiments confirm the basic picture derived from previous studies of Mn incorporation in (Ga,Mn)As and of the annealing process but the measurements are more direct and provide more detailed information about the structure of

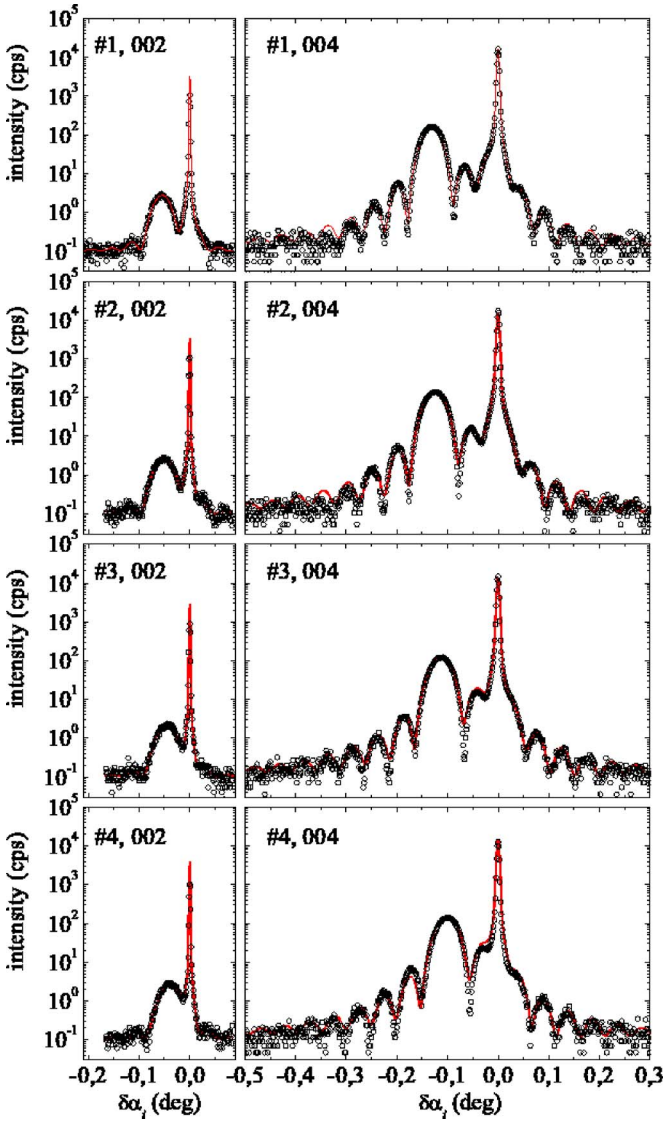

FIG. 9. (Color online) High-resolution x-ray diffraction curves of samples Nos. 1–4 in diffractions 002 (left column) and 004 (right column) (black points) and their fits by conventional dynamical diffraction theory (red lines).

the (Ga,Mn)As epilayer and of the layer surface. The XSW measurements clearly indicate the existence of a Mn_r-rich surface layer. The detailed chemistry of this layer is unknown to us; it could be a surface oxide growing during annealing of (Ga,Mn)As in air or a very thin MnAs layer.

The small number of $Mn_i^{(1)}$ we detected also requires further investigation. In particular, it would be useful to use a XSW geometry in which both $Mn_i^{(1)}$ and $Mn_i^{(2)}$ can be detected independently. Such a geometry together with calibration measurements on pure Mn crystal should allow for a fully quantitative interpretation of the XSW data. In order to detect $Mn_i^{(2)}$ independently of Mn_{Ga} atoms, it would be necessary to use a diffraction with a non zero out-of-plane component of the diffraction vector **h**, since Mn_{Ga} and $Mn_i^{(2)}$ atoms differ only in their vertical positions. For such a diffraction, the XSW effect can be measured (i) in the case of a very thin (Ga,Mn)As layer or (ii) for a very thick layer. In the

TABLE II. Lattice expansion parameters of the (Ga,Mn)As epilayers determined from the XRD measurements.

Sample No.	$\xi=\Sigma_{p=\mathrm{s,i,a}}\beta_p n_p$ (10^{-3} Å)	$(\beta_s n_s)$ (10^{-3} Å) for $\xi_a=0$	$(\beta_i n_i)$ (10^{-3} Å) for $\xi_a=0$	$(\beta_s n_s)$ (10^{-3} Å) for $\xi_a=5\times10^{-3}$ Å	$(\beta_i n_i)$ (10^{-3} Å) for $\xi_a=5\times10^{-3}$ Å
1	10.2±0.1	1.3±0.6	8.9±0.5	0.9±0.6	4.3±0.5
2	9.6±0.1	1.4±0.6	8.2±0.5	0.8±0.6	4.0±0.5
3	8.9±0.1	1.3±0.6	7.6±0.5	0.8±0.6	3.1±0.5
4	8.0±0.1	1.4±0.6	6.6±0.5	0.9±0.6	2.1±0.5

former case, the diffraction in substrate can be used for the creation of the standing wave and the (Ga,Mn)As layer has to be very thin so that the vertical misalignment of the Mn atoms (due to the lattice mismatch) with respect to the standing-wave pattern is negligible. This condition is fulfilled for the layer thickness

$$T \ll \frac{a_{\mathrm{sub}}}{f}, \tag{5}$$

where $f=(a_{\mathrm{layer}\perp}-a_{\mathrm{sub}})/a_{\mathrm{sub}}$ is the vertical lattice mismatch of the (Ga,Mn)As epilayer with respect to the GaAs substrate. Since in our case the mismatch is of the order of 10^{-2}, the (Ga,Mn)As layer would have to be much thinner than 50 nm.

In case (ii), the diffraction in the (Ga,Mn)As epilayer can be used as a source of the standing wave. In order to achieve a measurable XSW effect, the intensities of the primary and diffracted beams must be comparable; i.e., the thickness of the epilayer has to be comparable to the x-ray extinction length (above 1 μm). Note, however, that theoretical analysis of these experiments will be complicated by the fact that the standing wave itself is affected by the presence of Mn atoms.

VI. CONCLUSIONS

We have studied the structure of epitaxial (Ga,Mn)As layers and their changes during post-growth annealing using high-resolution x-ray diffraction and grazing-incidence x-ray standing-wave techniques. The layers are formed by a high-crystal-quality (Ga,Mn)As epilayer covered by a thin Mn-rich layer. We have identified that the excess surface Mn density is due to Mn atoms occupying random positions incommensurate with the host lattice. The increase of the density of random Mn atoms during annealing is correlated with the decrease of interstitial Mn density in the (Ga,Mn)As epilayer.

ACKNOWLEDGMENTS

We acknowledge fruitful collaborations with Tien-Lin Lee and other members of the beamline ID32 team at ESRF Grenoble and support from the Ministry of Education of the Czech Republic under Grants No. MSM 0021620834 and No. LC510, from the Grant Agency of Czech Republic under Grants No. 202/06/0025, No. 202/05/0575, and No. 202/04/1519, and from the UK EPSRC under Grant No. GR/S81407/01.

[1] F. Matsukura, H. Ohno, and T. Dietl, in *Handbook of Magnetic Materials*, edited by K. H. J. Buschow (Elsevier, Amsterdam, 2002), Vol. 14, p. 1.
[2] T. Jungwirth, J. Sinova, J. Mašek, J. Kučera, and A. H. MacDonald, Rev. Mod. Phys. **78**, 809 (2006).
[3] K. M. Yu, W. Walukiewicz, T. Wojtowicz, I. Kuryliszyn, X. Liu, Y. Sasaki, and J. K. Furdyna, Phys. Rev. B **65**, 201303(R) (2002).
[4] F. Máca and J. Mašek, Phys. Rev. B **65**, 235209 (2002).
[5] J. Blinowski and P. Kacman, Phys. Rev. B **67**, 121204(R) (2003).
[6] J. Mašek and F. Máca, Phys. Rev. B **69**, 165212 (2003).
[7] K. W. Edmonds, P. Boguslawski, K. Y. Wang, R. P. Campion, S. N. Novikov, N. R. S. Farley, B. L. Gallagher, C. T. Foxon, M. Sawicki, T. Dietl, M. B. Nardelli, and J. Bernholc, Phys. Rev. Lett. **92**, 037201 (2004).
[8] T. Jungwirth *et al.*, Phys. Rev. B **72**, 165204 (2005).
[9] T. Jungwirth *et al.*, Phys. Rev. B **73**, 165205 (2005).
[10] K. W. Edmonds, K. Y. Wang, R. P. Campion, A. C. Neumann, N. R. S. Farley, B. L. Gallagher, and C. T. Foxon, Appl. Phys. Lett. **81**, 4991 (2002).
[11] D. Chiba, K. Takamura, F. Matsukura, and H. Ohno, Appl. Phys. Lett. **82**, 3020 (2003).
[12] K. C. Ku *et al.*, Appl. Phys. Lett. **82**, 2302 (2003).
[13] M. B. Stone, K. C. Ku, S. J. Potashnik, B. L. Sheu, N. Samarth, and P. Schiffer, Appl. Phys. Lett. **83**, 4568 (2003).
[14] Y. Ishiwata, M. Watanabe, R. Eguchi, T. Takeuchi, Y. Harada, A. Chainani, S. Shin, T. Hayashi, Y. Hashimoto, S. Katsumoto, and Y. Iye, Phys. Rev. B **65**, 233201 (2002).
[15] F. Glas, G. Patriarche, L. Largeau, and A. Lemaitre, Phys. Rev. Lett. **93**, 086107 (2004).
[16] I. Frymark and G. Kowalski, J. Phys. D **38**, A160 (2005).
[17] J. Sadowski and J. Z. Domagala, Phys. Rev. B **69**, 075206 (2004).
[18] I. Kuryliszyn-Kudelska, J. Z. Domagala, T. Wojtowicz, X. Liu, E. Lusakowska, W. Dobrowolski, and J. K. Furdyna, J. Appl. Phys. **95**, 603 (2004).
[19] L. X. Zhao, C. R. Staddon, K. Y. Wang, K. W. Edmonds, R. P. Campion, B. L. Gallagher, and C. T. Foxon, Appl. Phys. Lett.

86, 071902 (2005).
[20] S. C. Erwin and A. G. Petukhov, Phys. Rev. Lett. **89**, 227201 (2002).
[21] D. E. Bliss, W. Walukiewicz, J. W. Ager III, E. E. Haller, K. T. Chan, and S. Tanigawa, J. Appl. Phys. **71**, 1699 (1992).
[22] J. Mašek, J. Kudrnovský, and F. Máca, Phys. Rev. B **67**, 153203 (2003).
[23] B. J. Kirby *et al.*, cond-mat/0602182 (unpublished).
[24] M. Adell, J. Kanski, L. Ilver, J. Sadowski, V. Stanciu, and P. Svedlindh, Phys. Rev. Lett. **94**, 139701 (2005).
[25] M. Malfait, J. Vanacken, W. Van Roy, G. Borghs, and V. V. Moshchalkov, Appl. Phys. Lett. **86**, 132501 (2005).
[26] B. J. Kirby, J. A. Borchers, J. J. Rhyne, K. V. O'Donovan, T. Wojtowicz, X. Liu, Z. Ge, S. Shen, and J. K. Furdyna, Appl. Phys. Lett. **86**, 072506 (2004).
[27] U. Pietsch, V. Holý, and T. Baumbach, *High-Resolution X-Ray Scattering from Thin Films and Lateral Nanostructures* (Springer-Verlag, New York, 2003).
[28] J. Zegenhagen, Surf. Sci. Rep. **18**, 202 (1993).
[29] I. A. Vartanyants and M. V. Kovalchuk, Rep. Prog. Phys. **64**, 1009 (2001).
[30] A. Authier, *Dynamical Theory of X-Ray Diffraction*, Vol. 11 of *International Union of Crystallography Monographs on Crystallography* (Oxford University Press, Oxford, 2001).
[31] J. Mašek and F. Máca, Acta Phys. Pol. A **108**, 789 (2005).